Prediction of aerodynamics installation effects of USF using body force modeling and metric-based mesh adaptation

A. Petrucci Orefice*, C. Tarsia Morisco**, F. Alauzet**
Corresponding author: armandojanni.petrucci-orefice@safrangroup.com
* Safran Tech, 78772 Magny les Hameaux, France
** GammaO, Equipe Inria-ONERA, Centre Inria de Saclay, Université Paris-Saclay, 91120 Palaiseau, France

Abstract: Recent efforts to improve aircraft engine efficiency highlight the Unshrouded Single Fan (USF) architecture, which aims for better propulsive efficiency and reduced drag and weight through larger fan diameters and smaller nacelles. However, strong airframe–propulsor interactions pose industrial challenges from the early stages of design. CFD is used to limit experimental costs, but full aircraft–engine simulations remain expensive, leading to the adoption of reduced-order models such as actuator disks and body force methods.

In this work, we propose a novel approach that combines body force modeling with anisotropic mesh adaptation to achieve steady, mesh-converged RANS solutions for USF installations.

The method allows for steady simulations in the aircraft frame and ensures mesh convergence. By automatically identifying zones for treatment within a mesh adaptation framework, this feature-based approach simplifies mesh generation and effectively captures both body force zones and flow structures. The results show good agreement with meshed simulations and demonstrate the feasibility of this less costly alternative for installed USF evaluations.

Keywords: Body Force Modeling, Mesh adaptation, Unshrouded Single Fan, Installation effects.

1. Introduction

In recent years, there has been an increasing focus on improving aircraft engine efficiency, reducing potential losses, and improving component design.

As propulsive efficiency can be directly related to propellers diameter, an ultimately interesting configuration is represented by the Unshrouded Single Fan (USF) architecture: on one hand it allows maximizing the blade dimension, and on the other hand smaller nacelles minimize parasite drag and reduce the weight of the engine. Even if the USF architecture may be very appealing for such reasons, it has to be still consolidated from an industrial point view and represents a disruptive choice for any engine manufacturer willing to pursue this design direction [1].

One of the main challenges is represented by the strong interaction of such type of engine with the whole aircraft. One example is given by the impact on the aerodynamics performance due to the mutual interaction of the wing with the propulsion architecture, which is the object of the present work, but also other aspects may affect the final design such aeroacoustic, structural and aeroelastic evaluations. As a result, a great development effort is needed to ensure the target performance at any flight condition, with consequent testing needs.

In this perspective, CFD simulation results in a good tool for reducing experimental facilities costs and optimization loops for correctly estimating the aerodynamics performance [2, 3]. But even within such a context, CFD simulations targeting the evaluation of the engine in conjunction with the full aircraft may result prohibitive during the preliminary phases of the design.

One way of alleviating the computational cost of such kind of simulations is to use a surrogate/reduced order model being able to reproduce the effects of the propeller on the flow, e.g. in [4] and actuator disk model is used to reproduce propeller effects. A recent category of reduced-order methods is the body force method [5, 6]. This modeling approach relies on replacing the actual blades by a source term distribution, which reproduces the essential flow features, namely flow turning and entropy rise. This allows a significant cost reduction because the blades are not actually meshed and the resulting computation is steady even for inflow distortion cases and has been recently used, for example, in [7] for the assessment of aeropropulsive installation effects of Ultra High Bypass Ratio (UHBR) engines and in [8] for propeller applications.

This paper also demonstrates the efficiency of anisotropic mesh adaptation to capture the rich physics of turbulent flows induced by the propeller. Thanks to a sustained effort on anisotropic mesh adaptation methods [9], they have been extended successfully to turbulent flows modeled by the RANS equations. In [10], we proved that it is possible to achieve very accurate predictions on fully-unstructured adapted meshes composed only of tetrahedra. Moreover, we showed that the same accuracy can be obtained with a reduction of the mesh size by a factor of between 20 and 100 with respect to the best-practice expert-created meshes [11]. One other important result is that we are now able to achieve mesh-convergence even on complex 3D geometries such as commercial airplanes with high-lift systems [10, 11]. Consequently, the discretization error becomes negligible with respect to the physical-modeling error and, now, we are able to compare models rigorously.

Two main targets should be achieved with the proposed strategy: on one hand it will be possible to obtain steady simulations (RANS) in the aircraft frame thanks to the body force modeling of the propeller, on the other hand the mesh adaptation strategy will ensure the mesh-convergence of the solution. Being able to guarantee both targets at any flight conditions would represent a quite challenging task and at the best of authors' knowledge there are no other examples in literature making use of body force models in conjunction of mesh adaptation strategies to achieve such result.

The paper is outlined as follow. We first detail the body force modeling in Section 2. Then, the mesh-adaptive solution platform is presented 3. Finally, Section 4 demonstrates the efficiency of the proposed method on USF geometry.

2. Body force modeling

In present work, the body force model proposed by [5] and further developed by [6] is employed to replace the rotating the blade of the USF configuration while the stator, the pylon and the rest of the aircraft will be fully meshed.

Following a typical decomposition of blade forces, proposed in its seminal work by Marble [12], it is possible to define a contribution of the aerodynamic force which is *normal* to the local relative velocity and contributes to the work and another one which is *parallel* and is related to the losses by means of Crocco's theorem. A scheme of such blade force decomposition is depicted in Figure 1.

In [5] only the normal component of the force is modeled and writes as follows

$$\boldsymbol{f} = \boldsymbol{f}_n = \frac{1}{2}\rho W^2 \frac{N_b}{2\pi R |n_\theta|} 2\pi\delta \widehat{\boldsymbol{f}}_n \tag{1}$$

where the ^ symbol denotes unit vector of the given vector $\widehat{\boldsymbol{w}} = \boldsymbol{w}/\|\boldsymbol{w}\|$, $\boldsymbol{W} = \boldsymbol{V} - \boldsymbol{\omega} \wedge \boldsymbol{r}$ is the velocity in the blade relative frame with norm $W = \|\boldsymbol{W}\|$ and $\boldsymbol{\omega}$ is the blade rotation velocity, N_b is the number of blades, R the distance from the rotation axis, $\boldsymbol{n}$ is the vector normal to the camber line of the blade and $|n_\theta|$ its component along the azimuthal direction, $\frac{1}{2}\rho W^2$ is a dynamic pressure given by the relative

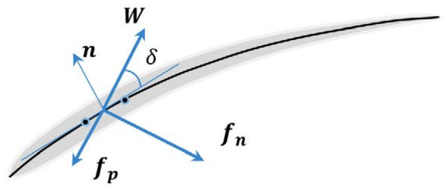

Figure 1: Blade force decomposition

velocity and finally the force is obtained by using a *local* flat plate analogy by replacing the angle of attack by the deviation angle in the lift coefficient solution of the flat plate, $c_l = 2\pi\alpha$.

In order to impose the normality to local relative velocity $\boldsymbol{W} \cdot \boldsymbol{f}_n = 0$ and the coplanarity with the plane defined by vectors $\boldsymbol{n}$ and $\boldsymbol{W}$, the unitary vector of the the normal force can be written as follows

$$\widehat{\boldsymbol{f}}_n = -\frac{(\boldsymbol{W} \wedge \boldsymbol{n}) \wedge \boldsymbol{W}}{||(\boldsymbol{W} \wedge \boldsymbol{n}) \wedge \boldsymbol{W}||} \quad (2)$$

and thus the deviation angle δ can be obtained by

$$\delta = \arcsin\left(\frac{\boldsymbol{W} \cdot \boldsymbol{n}}{W}\right) \quad (3)$$

In [6] the normal force is modified to accommodate compressibility and blockage effects by multiplying (1) by $\frac{K_{\mathrm{Mach}}}{b}$, where b is the blockage factor and K_{Mach} is a Prandtl-Glauert and Ackeret compressibility correction clipped at value equal to 3

$$K_{\mathrm{Mach}} = \begin{cases} \min\left(\dfrac{1}{\sqrt{1-M_r^2}}, 3\right) & \text{if } M_r < 1 \\ \min\left(\dfrac{4}{2\pi\sqrt{1-M_r^2}}, 3\right) & \text{if } M_r > 1 \end{cases}$$

A parallel force contribution is added as well

$$\boldsymbol{f}_p = \frac{1}{2}\rho W^2 \frac{N_b}{2\pi R |n_\theta|}\left(2C_f + 2\pi K_{\mathrm{Mach}}\left(\delta - \delta|_{\eta_{\max}}\right)^2\right)\widehat{\boldsymbol{f}}_p \quad (4)$$

where $\widehat{\boldsymbol{f}}_p = -\widehat{\boldsymbol{W}}$ as per definition, $C_f = 0.0592 Re_x^{-0.2}$ is the turbulent friction coefficient obtained for the flat plate expressed as a function of the local Reynolds number $Re_x = \rho W x/\mu$. The term related to the difference $\left(\delta - \delta|_{\eta_{\max}}\right)$ is described as an *off-design* loss term which needs to be calibrated on the targeted geometry. In particular $\delta|_{\eta_{\max}}$ is the deviation angle for the maximum efficiency $\eta_{\max}$.

3. Mesh-adaptive solution platform

Mesh adaptation is a non-linear problem where the couple formed by the mesh and the solution is converged at the same time. The goal is to generate the optimal adapted mesh for the computed solution for a prescribed mesh size (*i.e.,* a prescribed number of vertices). The simulations are performed with the mesh-adaptive solution platform composed of the flow solver Wolf [13], the anisotropic local remeshing software Feflo.a [14], the solution field interpolator Interpol [15] and the error estimate computation software Metrix [9] [10].

For the metric-based anisotropic mesh adaptation, an iterative process is required which is achieved by means of a mesh adaptation loop starting from an initial mesh $\mathcal{H}_0$, an initial solution W_0, and a given mesh size $\mathcal{N}$. At each step of the mesh adaptation loop, a metric tensor $\mathcal{M}_i$ is computed from the couple $(\mathcal{H}_i, W_i)$ and the given mesh size $\mathcal{N}$, using the selected error estimate. The metric tensor field $\mathcal{M}_i$ contains information on sizes and directions of the elements of the adapted mesh we seek. This information is then used by the remesher to generate a new adapted mesh $\mathcal{H}_{i+1}$. Then, W_i is interpolated on $\mathcal{H}_{i+1}$ to obtain $(W^0)_{i+1}$ which is then used as a restart solution for the next flow solution of the mesh adaptation loop. Restarts are important not to waste time in the adaptive process and to reuse the previous work done as much as possible. Finally, a new solution field W_{i+1} is computed. Solution fields are converged to machine zero (or close to machine zero) at each computation. The convergence criteria of the mesh adaptation loop is up to the expectations of the user who specifies when the couple mesh-solution is considered as converged for the current mesh size.

In the context of a mesh convergence analysis, this adaptation loop has to be repeated for several increasing mesh sizes $\{\mathcal{N}^j\}_j$. An efficient strategy consists in converging the couple mesh-solution for a given mesh size and reuse the final mesh and solution to initialize the next computations at an increased mesh size. Such a process enables a multiscale resolution of the flow by capturing large-scale features on coarse adapted meshes (at the smallest mesh sizes) and the fine scale features of the flow on fine adapted meshes (at the largest mesh sizes). This acts like a "multigrid effect" and enables faster convergence on fine adapted meshes.

Error estimates. Denoting by $\mathcal{M}_{\text{Opt}}$ the optimal metric, $C(\mathcal{M}_{\text{Opt}})$ its complexity (*i.e.* the continuous counterpart to mesh size), $\mathcal{N}$ the targeted complexity, and $\mathcal{E}$ the error model for the considered application, the problem to solve is

$$\mathcal{M}_{\text{Opt}} = \underset{C(\mathcal{M})=\mathcal{N}}{\text{argmin}}\ \mathcal{E}(\mathcal{M}).$$

The optimal metric field $\mathcal{M}_{\text{Opt}}$ used to prescribe the new adapted mesh $\mathcal{H}$ is automatically deduced from the actual solution or from the actual solution and adjoint state with different error estimates [13]. *Feature-based* error estimate aims at minimizing the interpolation error in L^p norm of a given sensor for a given number of degrees of freedom. It is easy to implement as it only requires the second derivatives of the sensor. For RANS simulations, we have shown that for most of the aeronautic applications a control of the L^4 norm of the interpolation error based on the local Mach number variable is very effective [16]. This is also the case for compressors in turbomachinery applications [13]. *Goal-oriented* error estimate minimizes the error of a given engineering scalar output functional for a given number of degrees of freedom. This error estimate is more complex and requires to compute the adjoint state.

Flow solver. Wolf is a vertex-centered second-order accurate mixed finite-volume - finite-element Navier-Stokes solver on unstructured meshes composed of tetrahedra in 3D. To improve spatial accuracy, a specific low dissipation finite-volume scheme is considered. The time integration implements an implicit temporal discretization. In particular, at each time step, the linear system is approximately solved using Symmetric Gauss-Seidel (SGS) relaxations, and local time stepping with local CFL is used to accelerate the convergence to steady state. As for the turbulence model, the negative Spalart-Allmaras (SA-Neg) is loosely-coupled to the mean-flow equations, where the mean-flow and turbulence model equations are relaxed in an alternating sequence. The Spalart-Allmaras turbulence model has been chosen because it is well-posed numerically, in the sense that the numerical method can converge the residual of the turbulence variable toward machine-zero similarly to the mean flow variables. This is fundamental to be confident with the obtained numerical solution. Moreover, the Spalart-Allmaras turbulent variable has a good behavior near the wall which makes this model very robust and compatible with the mesh adaptation workflow where the distance to the wall of the first layer of elements varies and is given solely by the error estimate. The flow solver Wolf is thoroughly detailed in [10, 13].

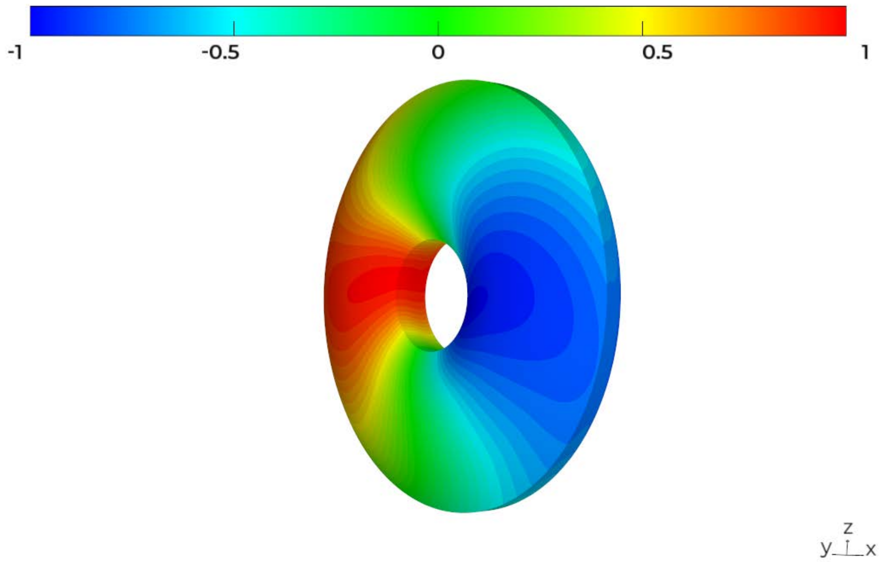

Figure 2: Body force support domain and z-component of normal vector, n, for NextAir rotor blade geometry

Local adaptive remesher. Feflo.a is a generic-purpose adaptive mesh generator dealing with 2D, 3D and surface mesh generation. It belongs to the class of metric-based mesh generators which aims at generating a unit mesh with respect to a prescribed metric field $\mathcal{M}$. The adaptive remesher uses on a combination of generalized standard operators (insertion, collapse, swap of edges and faces). The generalized operators are based on recasting the standard operators in a cavity framework [17]. During surface remeshing, either a P3 background surface is used [18] or direct CAD queries.

Coupled body force and metric-based mesh adaptation strategy In typical body force applications the zone of the domain where the source terms are applied is treated independently to conform to body force requirements; practically a dedicated block is created in the domain, usually structured, e.g. as described in [7].
In present work a different approach is proposed. A support domain, for example as in figure 2, is used to store the spatial data used by the body force model (e.g. the blade normal field, $\boldsymbol{n}$), and data are interpolated into the computational domain before the start of the simulation. This results in an *identification by interpolation* of the mesh volumes treated by the body force model, i.e. source terms of the model will be zero where no interpolated body force data are present.
Since such interpolation is performed before each simulation in the mesh adaptation process, it benefits of the mesh adaptation. In particular it is possible to see in next section that the process is able to *automatically* identify the body force zone in the domain by increasing the refinement in the boundaries of such zone, which conforms with the heuristic strategy adopted in classical body force simulations.

4. Numerical results

The USF geometry evaluated in present work is developed by Onera in collaboration with Safran within the NextAir European project [19]. It is composed by a rotor of 13 blades and stator of 11 blades. The flight condition for the design point is detailed table 1. Such data are used to setup all the simulations.

Design point	Flight conditions		
Cruise	M	=	0.75
	Alt	=	35 000 ft
	T	=	ISA + 0 K
	RPM	=	850

Table 1: Design point for the NextAir USF geometry

4.1 Meshed rotor simulations

Firstly, simulations of the isolated rotor blade were carried out to obtain reference values for the flow field. The simulations were performed in a rotating reference frame fixed to the blade, however, the RANS equations are expressed in terms of *absolute* velocity.

For this reason source terms must be included in the momentum equation to account for the non-inertial reference frame. Additionally, Arbitrary Lagrangian-Eulerian (ALE) fluxes must be computed to account for the mesh velocity.

The mesh adaptation process is started with an initial mesh with approximately 200 000 vertices, while final adapted mesh accounts for 12 800 000 vertices. For the mesh adaptation criterion, we consider the feature-based approach controlling the L^4 norm of the interpolation error on the local Mach number.

In figure 3(a,b) non dimensional values of pressure and z velocity component are shown; Mach number field is shown in figure 3(c) along with the final adapted mesh, 3(d) . It is possible to appreciate the tip vortex structures and rotor wake evolution and the underling mesh adaptation. Pressure field on the blade exhibits coherent shock structure on the suction side of the blade and adapted stagnation point on the pressure side.

4.2 Body force simulations of the isolated rotor

Body force simulations of the isolated rotor blade were carried out to perform comparisons against the reference results in the previous paragraph.

The mesh adaptation process is started with an initial mesh with approximately 100 000 vertices, while final adapted mesh accounts for 800 000 vertices. The difference in degrees of freedom with respect to meshed blade simulations is explained by the absence of the blade geometry in the domain. Nevertheless, the same mesh adaptation criterion is adopted, i.e. we consider the feature-based approach controlling the L^4 norm of the interpolation error on the local Mach number.

In figure 4(a,b) non dimensional values of pressure and z velocity component are shown; Mach number field is shown if figure 4(c). Three dimensional flow structures, such as tip vortices are not present in such simulations, which is coherent with the underling body force modeling hypotheses, based on an azimuthally averaged effects on the flow. Notwithstanding, overall pressure and Mach number distribution, along with the averaged value of azimuthal velocity component, are coherent with reference simulations which validates the suitability of the body force model expressed by (1) for the given geometry.

4.3 Body force simulation of USF

Finally, simulations of the complete USF geometry are carried out. Geometry used for such simulations is shown in figure 5 where the stator, composed of 11 blades, is represented while the rotor is not: it is added to the simulation via the body force model. This allows for steady RANS simulations for an otherwise unsteady case.

The mesh-adaptive solution process is started from an inviscid mesh without any boundary layer mesh nor any specific refinement for viscous flows. It is thus very easy and quick to generate. No meshing

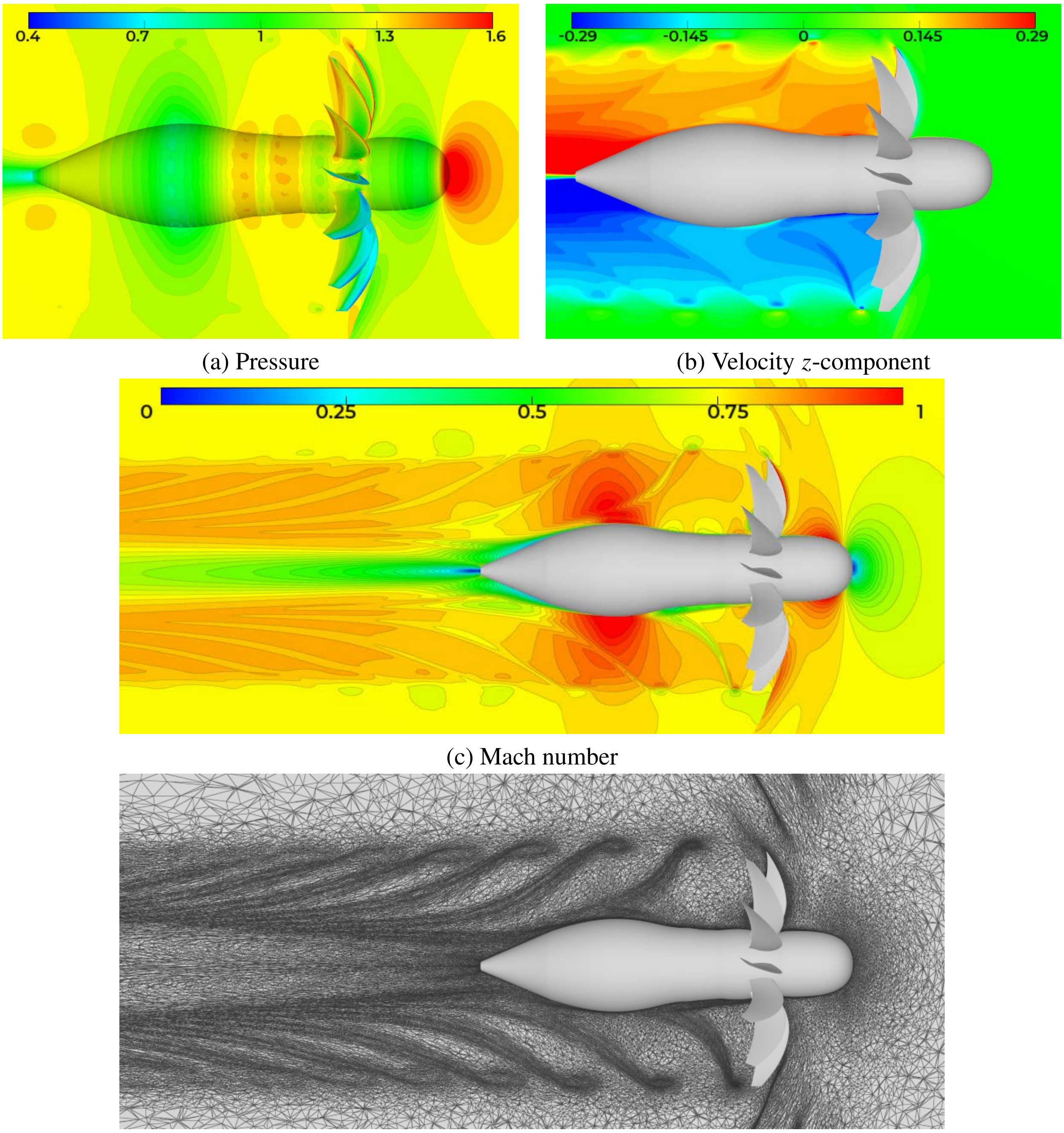

(a) Pressure

(b) Velocity z-component

(c) Mach number

(d) Adapted mesh

Figure 3: Final adapted solution: (a) non-dimensional pressure, (b) z-component of non-dimensional velocity vector, (c) Mach number, (d) adapted mesh for the rotor geometry of NextAir project in cruise conditions in the plane $z = 0$.

guidelines have been used. The starting mesh is composed of 3 703 555 vertices, 17 111 785 tetrahedra and 3 240 016 triangles on the surface, see Figure 6. It is a quite large starting mesh because we haven't unrefined the initial provided surface mesh, however the volume mesh is pretty coarse. For the mesh adaptation, we consider the feature-based approach controlling the L^4 norm of the interpolation error on the local Mach number. The mesh-adaptive process has been run up to adapted meshes composed of 6.5 millions vertices, 40 millions tetrahedra, and 1 millions triangles on the surface. The mesh-convergence study is performed by considering seven mesh sizes from 100K to 6.5M vertices.

The final adapted mesh and the final solution obtained for the cruise condition are shown in Figures 7, 8

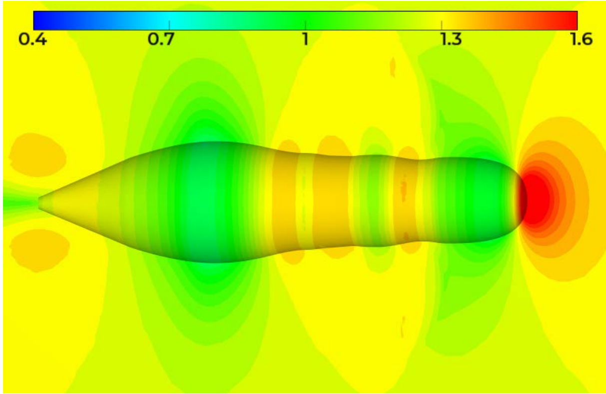

(a) Pressure

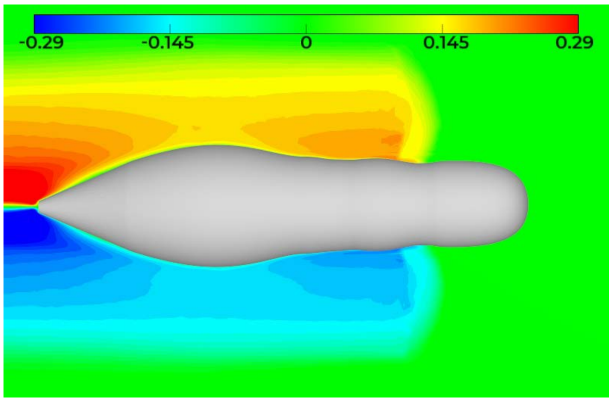

(b) Velocity z-component

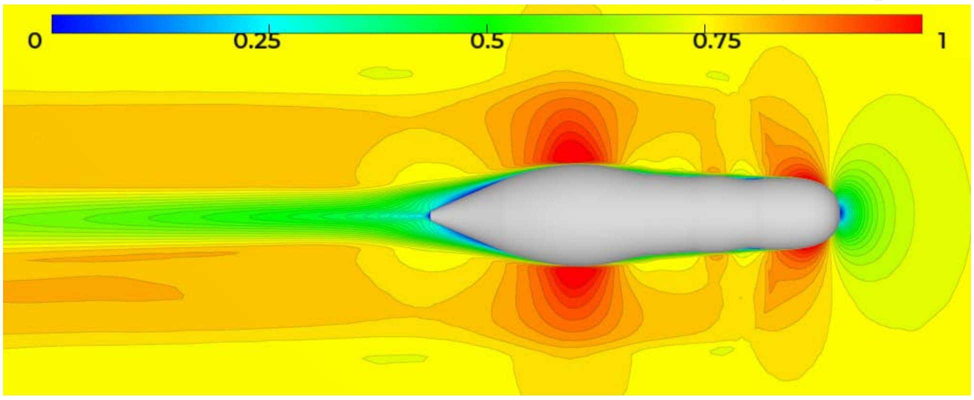

(c) Mach number

Figure 4: Final adapted solution: (a) non-dimensional pressure, (b) z-component of non-dimensional velocity vector, (c) Mach number, for the rotor geometry of NextAir project (body force model) in cruise conditions in the plane $z = 0$.

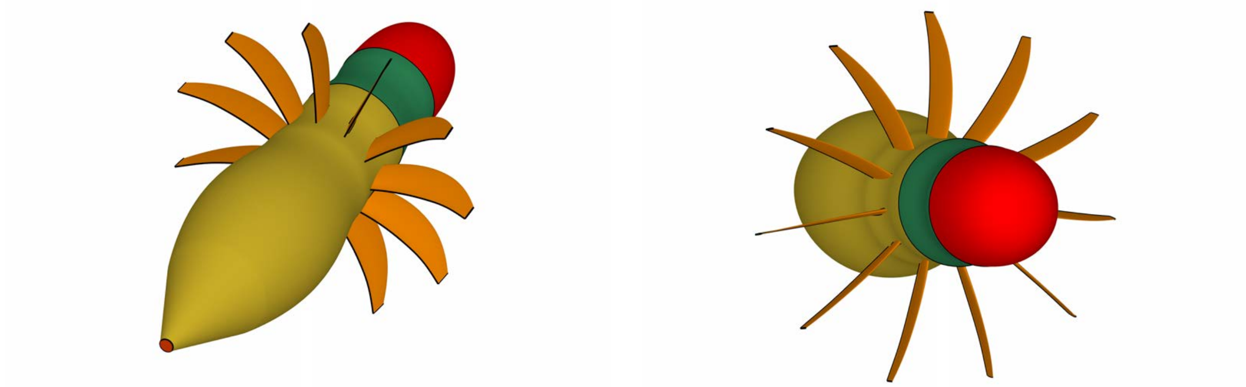

Figure 5: USF (stator and nacelle) geometry of NextAir project.

and 9.

Figure 7 shows the adapted mesh in the USF wake and the associated local Mach number in the plane $y = 0$. We saw complex flow patterns interactions notably between the nacelle wake and the stator blades wakes. The mesh adaptive process captures these complex patterns and mesh them appropriately to ensure accuracy. Moreover it automatically highlights the zone of the computational domain treated by the body force model as it is possible to observe the rotor blade shape in the adapted mesh.

Figures 8 and 9 depict the adapted mesh and each component of the velocity vector in the plane $x = -31$ and $x = -33$. It points out that the body force model imposes a high thrust, *i.e.,* high u-component of

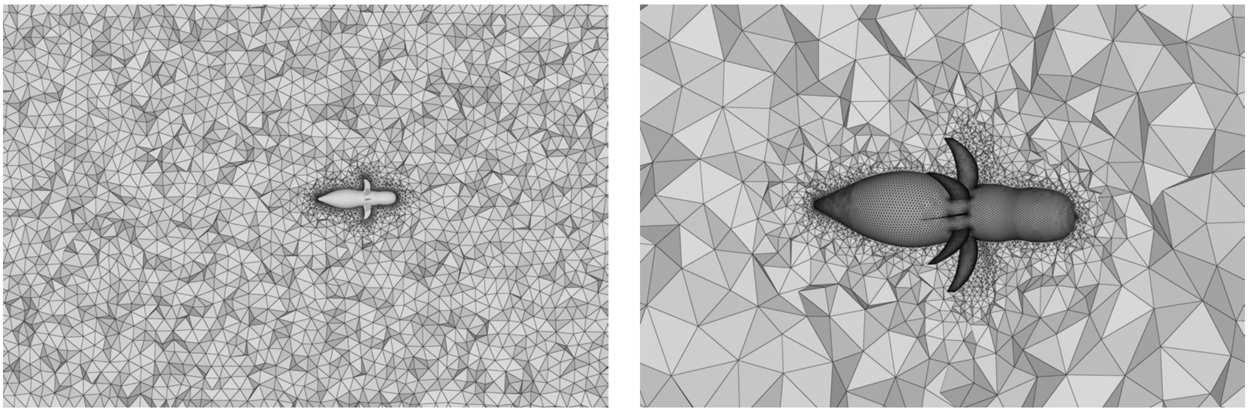

Figure 6: USF (stator and nacelle) geometry initial uniform mesh.

the velocity, and a counter-clockwise rotating flow shown by the v-component and w-component of the velocity. Again, the mesh is adapted accordingly to capture accurately all the wakes.

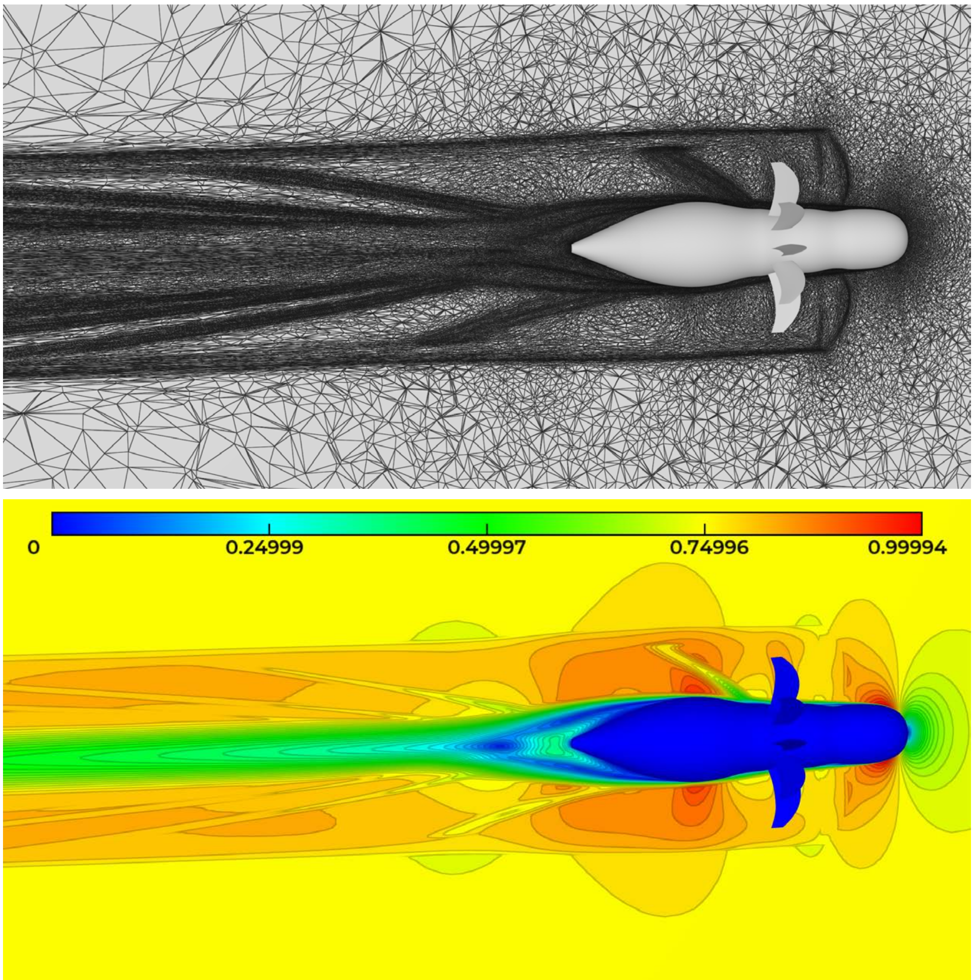

Figure 7: Final adapted mesh and final solution (local Mach number) for the USF geometry of NextAir project in cruise conditions in the plane $y = 0$.

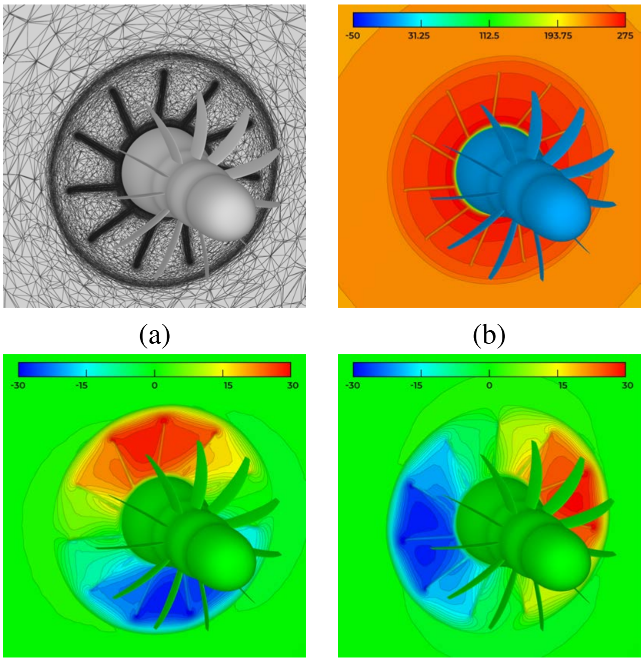

(a) (b) (c) (d)

Figure 8: Final adapted mesh and final solution for the USF geometry of NextAir project in cruise conditions in the plane $x = -31$. (a) final adapted mesh, (b) u-component of the velocity, (c) v-component of the velocity, and (d) w-component of the velocity.

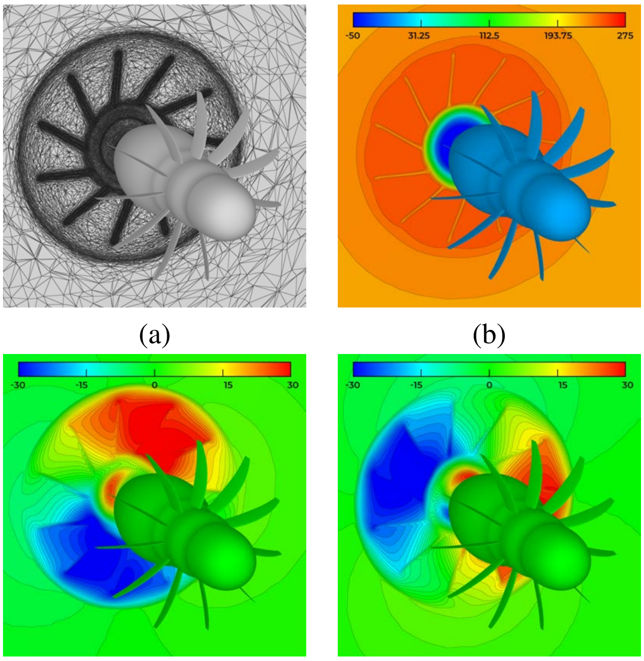

(a) (b) (c) (d)

Figure 9: Final adapted mesh and final solution for the USF geometry of NextAir project in cruise conditions in the plane $x = -33$. (a) final adapted mesh, (b) u-component of the velocity, (c) v-component of the velocity, and (d) w-component of the velocity.

5. Conclusions

In the present work, the application of body force modeling within a mesh adaptation framework has been investigated for complex industrial geometries, such as the Unshrouded Single Fan. A novel approach, differing from conventional body force simulations, has been proposed for identifying the zones to be treated by the model. This method relies entirely on interpolation steps of an external domain containing body force input data, relieving the user from the need to create dedicated zones for the body force model. This choice is also beneficial for the mesh adaptation process, as it removes the necessity to manage multiple zones and their connectivity. The feature-based approach demonstrated consistent results in capturing both the body force zone and the flow structures in the rest of the domain.

In particular, it was able to automatically identify the blade region and propose refinement at the boundaries of the body force cells, in accordance with best practices for meshing such kind of simulations. Comparisons between meshed and modeled rotor blade simulations showed good agreement, within the limits of the body force modeling assumptions, across different flow fields. Finally, complete USF simulations demonstrated the feasibility of applying this methodology to cases where rotor-stator interactions would otherwise require unsteady simulations, offering a less costly alternative for these types of evaluations. Despite the lower fidelity assumptions of the body force model, these simulations were able to capture the complexity of the stator wake and its interaction with the flow field originating from the stator, highlighting the promise of this tool for wing and airframe interaction studies as well.

References

[1] Karim Abu Salem, Giuseppe Palaia, Pedro D. Bravo-Mosquera, and Alessandro A. Quarta. A Review of Novel and Non-Conventional Propulsion Integrations for Next-Generation Aircraft. *Designs*, 8(2), 2024.

[2] Arne W. Stuermer. Validation of Installation Effect Predictions through Simulations of Contra-Rotating Open Rotors at Low-Speed Flight Conditions. In *33rd AIAA Applied Aerodynamics Conference*, AIAA AVIATION Forum. American Institute of Aeronautics and Astronautics, June 2015.

[3] Arne W. Stuermer. Validation of uRANS-Simulations of Contra-Rotating Open Rotor-Powered Aircraft at Take-Off Conditions. In *2018 AIAA Aerospace Sciences Meeting*, AIAA SciTech Forum. American Institute of Aeronautics and Astronautics, January 2018.

[4] F. Moens and P. Gardarein. Numerical simulation of the propeller/wing interactions for transport aircraft. In *19th AIAA Applied Aerodynamics Conference*, Fluid Dynamics and Co-located Conferences. American Institute of Aeronautics and Astronautics, June 2001.

[5] D. K. Hall, E. M. Greitzer, and C. S. Tan. Analysis of Fan Stage Conceptual Design Attributes for Boundary Layer Ingestion. *Journal of Turbomachinery*, 139(071012), March 2017.

[6] William Thollet, Guillaume Dufour, Xavier Carbonneau, and Florian Blanc. Body-force modeling for aerodynamic analysis of air intake – fan interactions. *International Journal of Numerical Methods for Heat & Fluid Flow*, 26(7):2048–2065, January 2016. Publisher: Emerald Group Publishing Limited.

[7] Andrea Magrini and Ernesto Benini. Aeropropulsive assessment of engine installation at cruise for UHBPR turbofan with body force fan modelling. *Aerospace Science and Technology*, 132:108048, January 2023.

[8] Thibaut Kiffer, Guillaume Dufour, Romain Gojon, William Thollet, and Luis López de Vega. Extension and validation of the Body Force Method to a propeller blade. In *AIAA AVIATION 2023 Forum*, AIAA AVIATION Forum. American Institute of Aeronautics and Astronautics, June 2023.

[9] F. Alauzet and A. Loseille. A decade of progress on anisotropic mesh adaptation for Computational Fluid Dynamics. *Comput. Aided Des.*, 72:13–39, 2016.

[10] F. Alauzet and L. Frazza. Feature-based and goal-oriented anisotropic mesh adaptation for RANS applications in aeronautic and aerospace. *J. Comp. Phys.*, 439(110340):77 pages, 2021.

[11] F. Alauzet, F. Clerici, A. Loseille, C. Tarsia-Morisco, and J. Vanharen. Some progress on CFD high lift prediction using metric-based anisotropic mesh adaptation. In *AIAA SCITECH 2022 Forum*, AIAA Paper 2022-0388, Jan 2022.

[12] Frank E Marble. Three-dimensional flow in turbomachines. In *Aerodynamics of Turbines and Compressors. (HSA-1)*. 1964.

[13] F. Alauzet, L. Frazza, and D. Papadogiannis. Periodic adjoints and anisotropic mesh adaptation in rotating frame for high-fidelity RANS turbomachinery applications. *J. Comp. Phys.*, 450(110814):65 pages, 2021.

[14] A. Loseille and R. Löhner. Cavity-based operators for mesh adaptation. In *51th AIAA Aerospace Sciences Meeting*, AIAA Paper 2013-0152, Dallas, TX, USA, Jan 2013.

[15] F. Alauzet. A parallel matrix-free conservative solution interpolation on unstructured tetrahedral meshes. *Comput. Methods Appl. Mech. Engrg.*, 299:116–142, 2016.

[16] A. Balan, M.A. Park, K. Anderson, D. Kamenetskiy, J. Krakos, T. Michal, and F. Alauzet. Verification of anisotropic mesh adaptation for turbulent simulations over ONERA M6 wing. *AIAA Journal*, 58(4):1–16, 2020.

[17] A. Loseille, F. Alauzet, and V. Menier. Unique cavity-based operator and hierarchical domain partitioning for fast parallel generation of anisotropic meshes. *Comput. Aided Des.*, 85:53–67, 2017.

[18] R. Feuillet, O. Coulaud, and A. Loseille. Anisotropic error estimate for high-order parametric surface mesh generation. In *Proceedings of the 28th International Meshing Roundtable*, Buffalo,

NY, USA, Oct 2019.

[19] Marco Carini. The NEXTAIR project: an overview of challenges and objectives. In *EUROGEN 2023*, 2023.